Biomaterials Science

PAPER

View Article Online
View Journal

Cite this: DOI: 10.1039/d6bm00185h

Biomimetic characterization by micro-computed tomography (μCT) of 3D hollow fibre membrane network bioreactors for tissue engineering

Giuseppe Falvo D'Urso Labate,[a] Chiara Morano,[b] Thomas De Schryver,[c] Harry Zaverdas,[d] Luigi De Napoli,[b] Gionata Fragomeni,†[e] Luc Van Hoorebeke,[c] Patrick Segers,[f] Matthieu N. Boone,[c] Konstantinos Theofilatos,[d] Joerg C. Gerlach[g] and Gerardo Catapano *[b]

Received 8th February 2026, Accepted 29th April 2026

DOI: 10.1039/d6bm00185h

rsc.li/biomaterials-science

Hollow Fiber Membrane Bioreactors (HFMBs) support mammalian cell culture at high cell density by enabling effective transport of nutrients, gases and metabolites to/from cells and by offering high membrane surface area-to-bioreactor volume ratios, scalability and flexibility in design. A recent study showed that shell-and-tube HFMBs with cells in the extracapillary space (ECS) for medicine may be designed to mimic the bone architecture for bone tissue engineering (TE). A more transport-efficient HFMB, the BRx-HFMB, consists of a 3D stack of alternating cross-woven mats of microporous and gas-permeable hollow fiber membranes with cells in the ECS and medium flowing inside the membranes. This design was shown to support the culture of a large mass of densely packed cells with high oxygen and nutrient metabolic demands similar to bone cells. Its biomimicry and rationale for good performance are poorly characterized, hindering exploitation of its characteristics for bone TE. Herein, we report the architectural and biomimetic characterization of pore/void distribution in the ECS of laboratory BRx-HFMBs using non-invasive non-destructive micro-computed tomography and advanced image analysis to minimize artifacts. The results suggest that the ECS pore architecture and specific surface area of BRx-HFMBs mimic those of bone tissue, favoring cell migration around, and adhesion on, membranes at clinical cell densities. The membrane network architecture enables cell perfusion with medium, and membranes act as spatially distributed oxygen sources promoting oxygen transport through the cell construct over longer distances than in static bioreactors. This supports the use of BRx-HFMBs to develop cellular models of bone tissue for drug testing and precision medicine.

1. Introduction

Hollow Fiber Membrane Bioreactors (HFMBs) were first proposed in 1972 for the co-culture of mammalian cells at quasi-*in vivo* density.[1] Since then, they have been slowly becoming an established upstream technology for mammalian cell culture in biomedicine.[2–6] They enable cell culture and co-culture at high density and the effective and selective transport of nutrients, dissolved gases and metabolites to/from the cells, protect sensitive cells from fluid-mechanical stresses, feature high membrane surface area-to-bioreactor volume ratios, and minimize contamination risks.[5–7] They are also cost-effective, easily scalable up and down, and flexible in design and operation. So far, their flexibility in design has been mainly exploited in technical applications, such as in wastewater treatment processes.[8,9] In substitutive and regenerative medicine,

---

[a] *Cellex srl, Piazzale delle Belle Arti 2, 00196 Roma, Italy. E-mail: giuseppe.falvodursolabate@cellex.it*
[b] *Department of Mechanical, Energy and Management Engineering, University of Calabria, Via Pietro Bucci, 87036 Rende (CS), Italy. E-mail: gerardo.catapano@unical.it, luigi.denapoli@unical.it, chiara.morano@unical.it*
[c] *UGCT-Rad. Phys., Dept. of Physics and Astronomy, Ghent University, Gent, Belgium. E-mail: thomasds@outlook.be, luc.vanhoorebeke@ugent.be, Matthieu.Boone@UGent.be*
[d] *InSyBio, Patras, Greece. E-mail: h.zaverdas@insybio.com, k.theofilatos@insybio.com*
[e] *Department of Medical and Surgical Sciences, Magna Graecia University, Catanzaro, Italy. E-mail: fragomeni@unicz.it*
[f] *BioMMedA, Institute of Biomedical Engineering, Department of Electronics and Information Systems, Ghent University, Campus UZ, Blok B – entrance 97, Corneel Heymanslaan 10, B-9000 Gent, Belgium. E-mail: patrick.segers@ugent.be*
[g] *University of Pittsburgh, Department of Surgery, UPMC Presbyterian Hospital F1281, 200 Lothrop Street, Pittsburgh, PA, 15213, USA. E-mail: jgerlach@pitt.edu*
† Present address: Department of Mechanical, Energy and Management Engineering, University of Calabria, Via Pietro Bucci, 87036 Rende (CS), Italy.

various bioreactors have been proposed to engineer biological substitutes of tissues or organs to replace missing or malfunctioning body parts or that are used in bioartificial organs to assist patients with metabolic insufficiency. Such a therapeutic strategy could be used in clinics to promote healing of tissues that regenerate, such as bone or the liver in fractured or acute liver failure patients, respectively, or to provide the missing synthetic functions in patients on extracorporeal artificial drug supplementation or blood detoxification treatments, such as diabetic or renal failure patients, respectively. Alternatively, tissue engineered cell substitutes could serve as personalized *in vitro* cellular models to screen drugs in substitution of animal testing.[10,11] To produce cell constructs that structurally resemble the natural tissue or organ, are metabolically competent, and match the size of the missing tissue/organ, organ or tissue-specific cells are isolated, seeded into a porous scaffold that replaces the natural extra-cellular matrix (ECM), and cultured in a bioreactor. There, they are challenged with time-varying paracrine and exogenous biochemical and fluid-mechanical cues that promote cell migration inside the scaffold, proliferation, differentiation, and reorganization in similar structures to the natural organ or tissue. Over the years, the importance of scaffold characteristics mimicking the natural ECM has become evident.[12] An ideal porous TE scaffold should present adherent cells with an architecture, dissolved and immobilized biochemical cues, and physical characteristics that mimic the natural ECM (*i.e.*, it should be biomimetic).[12–15] It is generally agreed that the architecture of TE scaffolds should feature a distribution of voids (hereinafter referred to as pores) characterized by: (1) a highly interconnected porous network similar to the natural tissue, to host a clinically relevant mass of cells at high physiological cell density and enable their reorganization as in the natural tissue; (2) a large scaffolding surface area, to permit adhesion of a large number of cells; and (3) a bimodal pore size distribution with pores larger than 300 μm, to permit cell migration into the innermost scaffold regions, and smaller pores a few microns large, to facilitate dissolved oxygen and nutrient supply to cells (as well as waste metabolite removal) anywhere in the scaffold and maintain cells viable and functional.[15,16]

Bone is a dynamic, hierarchical, highly heterogeneous natural composite differing from other tissues in the high percentage of the ECM, integrating organic and inorganic phases, and the low percentage of cells. Similar to the TE of other tissues, research in bone TE has been mainly focused on the development of porous scaffolds, made of polymers, metals, ceramics and glasses, or combined into hybrid scaffolds, mimicking the hierarchical architecture and morphology, and the mechanical, chemical and biochemical properties of the bone ECM, and that are osteoconductive (to permit colonization, migration, adhesion and proliferation of osteogenic, vascular and immune cells), osteoinductive (to recruit progenitor cells through biomolecular signalling and promote their differentiation) and osteointegrating (to enable the structural and functional connection of the cell construct with the bone of the recipient). Details on the many biomaterials and fabrication techniques proposed for bone TE may be found in the reviews available in the literature.[17–21] In the case of bone, maintaining the homeostasis of the bone microenvironment has been shown to be fundamental for bone regeneration and repair.[22–25] The bone microenvironment is characterized by a dynamic combination of physiological (*e.g.*, peculiar cell types, interactions among neighbouring cells and exchange of paracrine signals), chemical (*e.g.*, soluble nutrients, dissolved oxygen, proteins, hormones and signalling species, such as cytokines and VEGF), and physical aspects (*e.g.*, morphology, stiffness, porosity, and mechanical, fluid-mechanical or magnetic stimulation), all of which affect the metabolic behaviour of cells. To culture a cell construct in the presence of interplaying physiological, chemical and physical cues typical of the bone microenvironment, biomaterials have been developed that, in addition to mimicking the bone ECM, elicit controlled cell responses by varying their surface morphology, porosity, pore size distribution, wettability, charge and the presence of chemical functions, to quote but a few. Oxygen is a chemical signal that plays an important role in bone metabolism and regeneration and influences the balance between new bone formation by osteoblasts and resorption by osteoclasts.[26,27] Under normal physiological conditions, cells in the bone are cultured under hypoxic conditions. However, successful bone regeneration after an injury depends on well-defined changes of dissolved oxygen concentrations across time and space oscillating between a hypoxic phase (to recruit mesenchymal stem cells, to start angiogenesis and to favour chondrogenesis) and a reoxygenation phase (to favour osteoblast differentiation, to meet the high oxygen demand of osteoblasts and prevent cellular necrosis, to synthesize the ECM and mineralize it). Most bioreactors proposed for the culture of many of these scaffolds seeded with osteogenic cells cannot reproduce the bone microenvironment for oxygen. This has promoted the search for new bioreactors integrating biomimetic scaffolds and oxygen supply to mimic the bone microenvironment for oxygen.

Shell-and-tube HFMBs are the HFMBs more often used in medical applications. In these HFMBs, cells are seeded and cultured in the extra-capillary space (ECS) of a bundle of parallel hollow fibre membranes assembled in a closed housing/shell. Medium flows in the membrane lumina, as shown in Fig. 1a. In TE applications, shell-and-tube HFMBs may replicate cell organization around the local network of blood vessels and the mechanisms of oxygen supply typical of natural tissues like bone and the liver.[28] The hollow fibre membranes scaffold the seeded cells in a similar fashion to the natural ECM, with cells organizing around the HF membranes as they would around blood vessels in some natural tissues. The medium flowing in the membrane lumen supplies dissolved oxygen and nutrients to tissue (and removes waste metabolites) similar to the blood circulating in the Haversian canals in the bone and the vessels of the portal triads in the liver *acinus*. From there, oxygen is transported radially to the cells around the membranes similar to the function performed by the Volkmann canals in the bone and the sinusoids spreading from the portal triads in the liver *acinus*. Model-driven

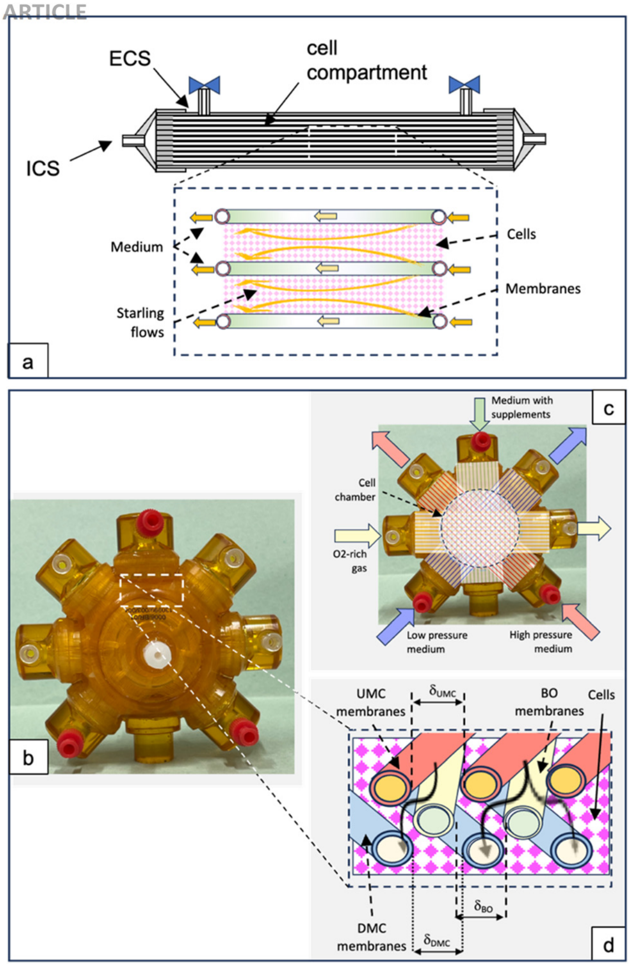

Fig. 1 Scheme of the BRx-HFMB – schematic comparison of the structures and operations of (a) the shell-and-tube hollow fiber membrane bioreactor (HFMB) operated in closed-shell mode; and (b–d) the 3D membrane network hollow fiber membrane bioreactor (BRx-HFMB) operated in perfusion mode – (b) structure and (c and d) operation.

approaches have been developed for closed-shell HFMB design in which nutrients, dissolved oxygen and metabolites are transported by pure diffusion[29–31] or solute transport is enhanced by spontaneously occurring Starling flows.[32–35] On this account, HFMBs have been proposed for engineering bone tissue and for extra-corporeal assistance to malfunctioning liver tissue. Recently it was shown that the ECS of shell-and-tube HFMBs may feature a controlled pore distribution and architecture mimicking the natural bone only if they are equipped with rolled mats of cross-woven hollow fibre membranes.[36] Cell proliferation, to near *in vivo* density, and differentiation, accompanied by the secretion of ECM components, reduce the hydraulic permeability of the ECS. As the cell construct matures, this causes solute transport to cells to occur mainly by diffusion. This limits the pathlength over which nutrients and dissolved oxygen effectively diffuse into the cell construct and the mass of viable cells that can be cultured per unit HFMB volume. In these HFMBs, even when tissue-specific cells are co-cultured with endothelial cells (ECs), ECs may align and form neo-vessels in the ECS oriented in the direction of the Starling flows along the bioreactor axis (as shown in Fig. 1a). This limits perfusion in mature co-cultured constructs and cell survival and functions, reducing the therapeutic effectiveness of HFMBs, as has been often reported for bioartificial livers.[37,38]

A more transport-efficient HFMB design, today termed a mass exchanger hollow fibre membrane bioreactor (BRx-HFMB), was proposed in the early 1990s by Gerlach (Fig. 1b).[39] This bioreactor design, then considered unconventional, exploited the possibilities offered by the mats of cross-woven hollow fibre membranes with varying separation and physical–chemical properties originally developed for blood oxygenators.[40,41] As shown in Fig. 1b–d, the BRx-HFMB is a four-compartment HFMB consisting of a three-dimensional (3D) stack of repeating flat modular units each made of pairs of cross-woven parallel microporous membrane mats for therapeutic plasmapheresis (TP) with an interposed cross-woven membrane mat for blood oxygenation (BO). Cells are cultured in the bioreactor ECS outside the membranes (*i.e.*, the ECS or cell compartment, CC). The membranes in each mat are rotated by about 45 degrees with respect to those in the adjacent mats, and the ends of each membrane type are bundled together, polyurethane is cast over them, and they are equipped with separate inlet and outlet headers, after cutting the membrane length excess with a sharp blade. Oxygen-rich gas flows through the lumina of the BO membranes (*i.e.*, the gas compartment, GC). Nutrients and oxygen-rich medium flow through the lumina of the two TP membrane mats.

The BRx-HFMB may be operated under a hydrostatic pressure difference between the medium compartments upstream (*i.e.*, the upstream medium compartment, UMC) and downstream (*i.e.*, the downstream medium compartment, DMC) of the cell layer. Under such conditions, the medium enters the bioreactor UMC, permeates the membrane wall at a controlled rate, bathes the cells (which consume nutrients and oxygen), flows outside and around the BO membranes (where it is enriched in the oxygen diffusing out of these membranes and depleted in carbon dioxide diffusing out of the medium and into the BO membranes), and eventually filters into the bioreactor DMC from where it leaves the bioreactor. The BRx-HFMB has been used for the culture and co-culture of cells with high oxygen and nutrient metabolic demands, such as primary human and porcine liver cells (proposed as the core of a bioartificial liver for assistance to liver failure patients),[42] and induced pluripotent and embryonic stem cells.[43–48] It has been shown that the co-culture of parenchymal and non-parenchymal liver cells in the BRx-HFMB ECS with a controlled medium flux perfusing the cell-seeded ECS could maintain a large mass of liver cells (up to 800 g)[49] viable at densities as high as 10^9 cells per mL (ref. 50) for several weeks and could even foster cell re-organization as in the natural liver and differentiation.[51] These characteristics make the BRx-HFMB appealing also for bone tissue engineering for the high metabolic demands of bone cells. Despite the reported interesting results, little attention has been paid to the characterization of the architectural and biomimetic properties of the pore (*i.e.*, void) distribution in the BRx-HFMB. This is likely due to the bioreactor complex structure and the structural damage caused (and the artifacts introduced) by invasive and destructive investigation techniques, such as embedding in paraffin followed by cutting with sharp blades. To the best of our knowledge, to date, quantitative information on the architecture and biomimicry of the BRx-HFMB ECS is still lacking.

To bridge this gap, in this paper we report on the structural and biomimetic characterization of the pore distribution in the ECS of laboratory-scale BRx-HFMB prototypes. Micro-computed tomography (μCT), a non-invasive and non-destructive analytical technique, coupled to advanced image analysis was used to minimize possible artifacts. We focused on the architectural features that influence cell migration, adhesion, and reorganization around the membranes. Biomimicry was evaluated by comparing these characteristics to those of natural equine femur tissue and a commercial hydroxyapatite scaffold used for bone TE and regenerative medicine.

2. Materials and methods

The methods used for this investigation are similar to those reported for previous investigations. For this reason, their description may resemble those reported by Falvo D'Urso Labate *et al.*,[36,52] occasionally *verbatim*.

2.1 The 3D membrane network bioreactor

Two laboratory-scale prototypes of BRx-HFMBs were used with a cell-chamber of a nominal 8 ml volume[53] which were kindly donated by Hybrid Organ GmbH (Berlin, Germany). The bioreactors were manufactured by casting a polyurethane housing around a 3D network of hollow fibre membranes consisting of a stack of flat repeating modular units made of overlaid alternating mats of cross-woven hollow fibre membranes for therapeutic plasmapheresis and blood oxygenation, as described above. In particular, the prototypes were equipped with mats of parallel cross-woven microporous polyethersulfone (mPES) HF membranes for TP featuring a 300 μm inner diameter, a 100 μm wall thickness and a 0.5 μm maximal pore size (3M, Wuppertal, Germany); mats of cross-woven microporous polypropylene (PP) Oxyphan™ HF membranes for BO featuring a 280 μm inner diameter, a 50 μm wall thickness, and a 0.2 μm maximal pore size (3M, Wuppertal, Germany); and a loose bundle of regenerated cellulose (RC) HF membranes for hemodialysis (HD) with an outer diameter of about 220 μm (3M, Wuppertal, Germany), as an additional spatially distributed route for separately delivering biochemical cues to the cells.

2.2 Characterization of the bioreactor ECS architecture

The architectural features of the intermembrane ECS voids outside and among the hollow fibre membranes (herein termed "pores") were characterized using micro-computed tomography and advanced image analysis techniques, as described below. In the analysis of images, the contribution of the intra-capillary space and the membrane walls to the ECS volume was excluded throughout. The architecture of the ECS was characterized in terms of its porosity ε, pore interconnectivity I_p, specific surface area a_v, and mean pore diameter d_{pm}, as described below. The reported values of the first three architectural parameters are averaged estimates in four volumes of interest (VOI) (one in each bioreactor quadrant in the y–z plane), in symmetrical positions with respect to the y–z and x–y planes passing through the cell seeding port, in both bioreactor prototypes (*i.e.*, $n = 8$). Each VOI was a cuboid with a square cross-section 5.85 × 5.85 mm^2 large, orthogonal to the

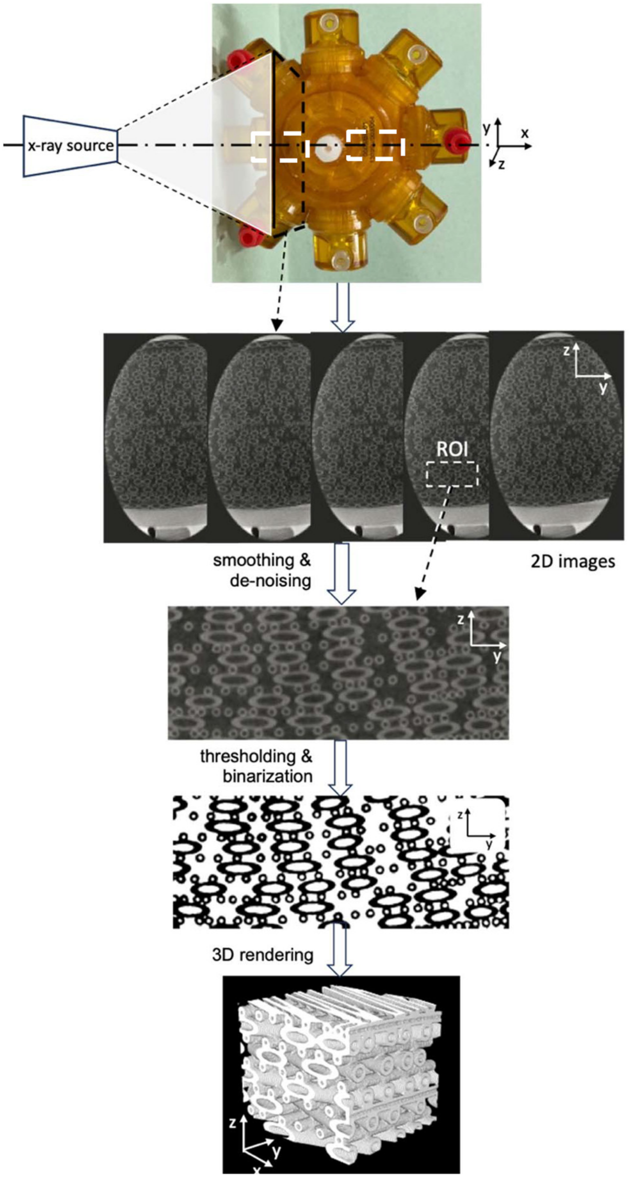

Fig. 2 Image acquisition and pre-processing – scheme of the bioreactor image acquisition procedure by μCT and of the image pre-processing procedure leading to the 3D reconstruction of the extra-capillary space of the BRx-HFMB. Approximate positions of VOI are shown as white dashed squares.

plane of the membrane mats (*i.e.*, the *y*–*z* plane in Fig. 2), and 3.7 mm long along the *x* axis (*i.e.*, parallel to the plane of the membrane mats). The values of the fourth parameter are averaged over at least five measures on five different 2D regularly spaced cross-sections in each VOI in both bioreactor prototypes (*i.e.*, n = 200). The size and location of the VOI were selected to make it possible to describe the 3D membrane network as a continuum (*i.e.*, the size of a VOI much greater than the membrane diameter) and to gather information representative of the microenvironment where cells are cultured (*i.e.*, the VOI large enough to be representative of the culture zone, yet small enough to permit characterization of the ECS architecture in the four quadrants of the bioreactor).

The biomimicry of the BRx-HFMB ECS was assessed with respect to bone tissue and potential bone substitutes by comparing the values of the bioreactor architectural parameters to those of the following three benchmarks: natural equine femur trabecular bone tissue (EFT); a commercial narrow pore hydroxyapatite scaffold (NPHA) used as a synthetic bone substitute (tradename EngiPore® – PFS015005-23-00); and a shell-and-tube HFMB equipped with densely packed cross-wound membrane mats (HDCW-HFMB). The architectural characteristics of these benchmarks are reported in Falvo D'Urso Labate *et al.* (2022 and 2016).[36,52]

2.3 Image acquisition and pre-processing

High-resolution μCT images of the BRx-HFMB ECS were acquired and pre-processed to facilitate their analysis according to the steps shown in Fig. 2. 2D images of the bioreactor cross-sections were obtained after scanning and reconstruction with the High-Energy CT system Optimized for Research (HECTOR), a μCT scanner specifically developed for research by the Ghent University Center for X-ray Tomography in collaboration with X-Ray Engineering (XRE bvba, Ghent, Belgium).[54] The X-ray source employed for the acquisition of 2D images was operated at a voltage of 140 kV and a current of 71 μA.

2D images were acquired on surfaces orthogonal to the plane of the membrane mats in the middle and at the two ends of each bioreactor (*i.e.*, n = 3). The pore architecture was reconstructed from the images acquired in the middle of the bioreactor, the most representative part of its structure. The isotropic voxel size typically ranged between 93 μm^3 and 103 μm^3. Generally, the 2D cross-sectional images were affected by significant levels of noise and poor contrast. Noise and contrast were optimized by subjecting images to smoothing and de-noising procedures with purposely developed AI-based algorithms written in Python organized in an image pre-processing pipeline consisting of established image-analysis methods implemented with the scikit-image and OpenCV libraries. The workflow included membrane masking, edge smoothing, quantitative comparison of candidate denoising filters, and filter selection based on residual noise minimization, as described in detail in the image pre-processing pipeline section. Then, the contrast-enhanced greyscale 2D images were thresholded and binarized and their 3D architecture was reconstructed with ImageJ (NIH, Bethesda, MA, USA)[55] at a threshold value equal to 33 (on a scale ranging from 0 to 255) to better distinguish solid parts from voids (*i.e.*, the pores). Finally, the architectural parameters were estimated either in the four VOIs shaped as cuboids with the axis parallel to the membrane mats (*x*-direction in Fig. 2), or on flat regions of interest (ROI) taken at regular distances from the outermost VOI cross-section, as described below.

2.4 Image pre-processing pipeline

The 2D images were pre-processed by applying the smoothing and de-noising pipeline schematically shown in SI Fig. S1. The procedure was initialized with the extraction of different subsets of images from the whole set of images for each bioreactor. Two cuboid VOI were identified in the middle of each bioreactor in a symmetrical position with respect to the sagittal plane of the bioreactor, with the axes parallel to the planes of the membrane mats (*i.e.*, the *x*-direction), over a length of 3.7 mm. Each VOI contained a stack of about 400 reconstructed 2D images. 10 images were randomly selected in each stack according to the stratified sampling procedure and were used as test samples to seek the most effective filter in reducing the inherent noise. The sampling procedure ensured the representation of all areas of each bioreactor. The test images were subjected to a sequence of pre-processing techniques to smooth the edges of the membrane cross-sections and to reduce their inherent noise. The procedures were developed and implemented by using the Python scikit-image[56] and OpenCV[57] library packages. As is often the case, it was assumed that the statistical noise derived from image acquisition is distributed according to a Gaussian probability density function,[58] as shown in eqn (1), where h is the additive white noise to a pixel, μ is the mean grey value, and σ is its standard deviation. σ provides information on the spread of the noise distribution, and it is indicative of the noise strength of the input signal:[59]

$$G(h) = \frac{1}{\sigma\sqrt{2\pi}} e^{-\frac{h-\mu^2}{2\sigma^2}} \tag{1}$$

The first step was to estimate the standard deviation of the Gaussian noise for each image in the 10-image stack, σ. In the second step, the edges of the membrane cross-sections were smoothed to avoid erratic uneven membrane surfaces in the 3D reconstruction of the various bioreactor parts. A mask was applied to distinguish the ring-like structure of the membranes from the background. The grey-scale nature of the images permitted the implementation of Otsu's thresholding to automatically categorize each pixel into white (the membrane) or black (the background).[60] Smoothing was performed only on the membranes by using OpenCV's Gaussian Blur function and by recombining the membranes with the background. In the third step, the filter was sought that was most efficient at reducing the inherent Gaussian noise, σ, of images among the following four filters: the Total Variation (TV) filter,[61] with weights 0.1 and 0.2; the Bilateral filter[62,63] with s = 0.05 and 0.1; the Wavelet filter;[64] and the Non-Local Means (NLM) filter.[65] The TV filter reduces the total variation of the signal to approximate the original signal, by keeping the edges and by removing unwanted details. The Bilateral filter preserves the edges by averaging pixels based on their spatial closeness and radiometric similarity. The Wavelet filter uses the wavelet representation of the image, where noise is represented by minuscule values in the wavelet spectrum, set to 0. The NLM filter preserves details and smooths a target pixel by using the weighted averages of all the pixels, rather than only the neighboring ones. The average inherent σ of noise in the selected 10 images was then calculated. Each denoising filter was applied to these 10 images and the average σ value was recalculated. The filter yielding the greatest reduction in σ was selected and used for de-noising all the other images in the stack of each VOI after they had been subjected to the same smoothing procedure described previously. The entire computational workflow was made available in the public GitHub repository (see the Data availability statement), inclusive of the Python notebook and user instructions for the sequence of preprocessing steps applied to the image stacks. After smoothing and de-noising, the gray-scale images were binarized with the ImageJ software (NIH, Bethesda, MA, USA) at a threshold value of 33 to distinguish between solid parts and voids (*i.e.*, pores). Finally, the 3D architecture of each VOI was reconstructed with ImageJ (NIH, Bethesda, MA, USA).

2.5 Image analysis

The pore architecture in each VOI/ROI was characterized in terms of selected parameters providing information on the ECS capacity to promote cell migration inside the 3D membrane network and cell adhesion on membrane outer surfaces and to effectively host a large clinical mass of cells and ensure sufficient nutrient supply (and waste removal) to maintain cells viable and functional. The parameters were also chosen to permit comparison with the characterization of the natural bone ECM and synthetic bone substitutes reported by Falvo D'Urso Labate *et al.*[52] and are briefly described below:

– ECS porosity, ε: the ECS porosity was defined as the fraction of the bioreactor volume occupied by the pores (*i.e.*, the voids); ε provides information on the volume (and also the mass and number) of cells that a bioreactor may host per unit bioreactor volume and was estimated as the ECS pore volume to total volume ratio of each VOI.

– Pore interconnectivity, I_p: the pore interconnectivity was defined as the fraction of the void volume that is connected with other voids in the ECS. I_p provides information on cell freedom to migrate everywhere in the ECS and was estimated as the fractional volume of open pores, or the complement to one of the fractional volumes of closed pores, in a VOI.

– Specific surface area, a_v: the specific surface area was defined as the area of solid surfaces in the ECS per unit bioreactor volume. a_v provides information on the solid surface area available for cell adhesion per unit bioreactor volume and was estimated as the outer membrane surface area to total volume ratio in each VOI.

– Mean pore diameter, d_{pm}: d_{pm} provides information on the ease with which cells may migrate into, or nutrients may flow across, the 3D membrane network and characterizes the sieving capacity of the 3D membrane network. For pores with irregular rectangular void cross-sections in the 2D images of the VOI cross-sections parallel to the membrane mats, d_{pm} was estimated as the diameter of the largest circle inscribed in the voids over five flat ROIs evenly distributed along the VOI length and orthogonal to its axis. For pores with long and thin slit cross-sections, d_{pm} was estimated from the 3D reconstruction of the membrane network in terms of the distance between adjacent membranes in a mat. Together with I_p, d_{pm} provides information on the bioreactor ECS capacity to enable unhindered transport of cells, nutrients, and paracrine and autocrine cues in all directions inside the 3D membrane network.

2.6 Statistical analysis

Data are reported as mean ± standard deviation. Microsoft Excel (Microsoft Corporation, Redmond, WA, USA) was used to check whether data were normally distributed. Unless otherwise indicated, the reported parameter values were averaged over all investigated ROIs, VOIs and prototypes. The statistical significance of residual noise differences in the same 10 stratified sampled images treated with various denoising filters was assessed with the non-parametric Friedman test, followed by Wilcoxon signed-rank *post hoc* tests with Holm correction for multiple paired comparisons. This choice was based on the paucity of data and the skewed distribution of residual-noise values across methods. The statistical significance of mean pore diameter differences in various bioreactor quadrants was assessed with a one-way analysis of variance (ANOVA). The statistical significance of differences of porosity, interconnectivity and specific surface area in the various bioreactor quadrants was assessed with the non-parametric Kruskal–Wallis test for the limited number of available measurements. In all cases, the level of statistical significance was set at $p < 0.05$ (two-sided in the case of filter noise reduction).

3. Results and discussion

The existing knowledge gap in BRx-HFMB architectural characteristics was addressed by characterizing the pore architecture and biomimicry of the bone tissue of the ECS of laboratory-scale BRx-HFMB prototypes. To minimize the introduction of artifacts, we used μCT, a non-invasive and non-destructive investigation technique, coupled with advanced image analysis.

3.1 Image acquisition and pre-processing

Fig. 2 schematically outlines the steps through which they were pre-processed. The reconstructed 2D slices of the BRx-HFMBs exhibited poor contrast and significant inherent noise (Fig. 3a and b). To minimize possible visual artifacts, a Python-based batch image preprocessing pipeline was developed to enhance image contrast by smoothing the edges of the membranes and reducing the inherent noise. This was expected to facilitate the reconstruction of the pore architec-

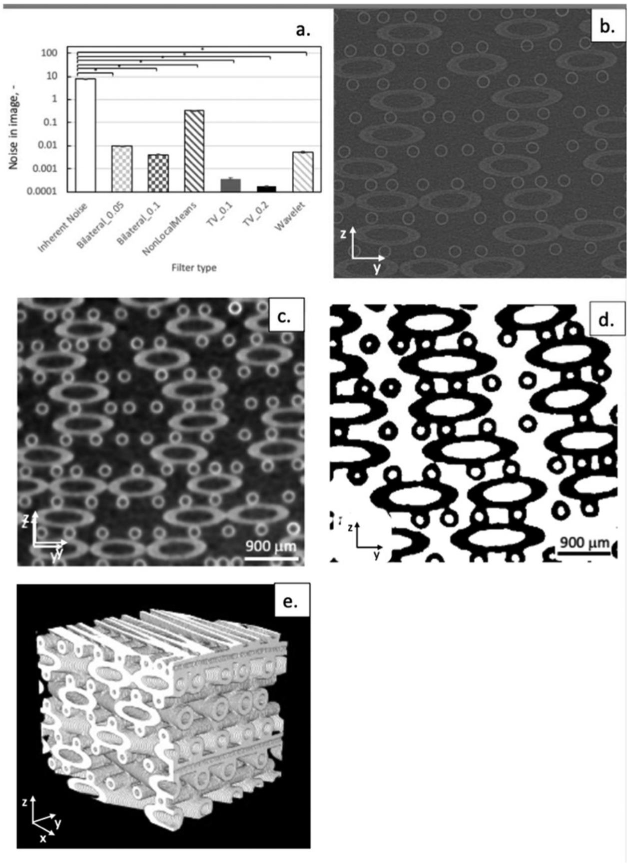

Fig. 3 Effects of the Python-based image pre-processing pipeline. Contrast enhancement of bioreactor raw 2D scanned images achieved by the pre-processing workflow: (a) comparison of residual noise reduction after application of the candidate denoising filters to the same set of images (see text for the filter description); (b) exemplary raw 2D image; (c) exemplary image after the smoothing and de-noising procedure; (d) exemplary image after the thresholding and binarization procedure; and (e) still image of the 3D reconstructed ECS architecture.

ture and its analysis. All investigated digital filters reduced the inherent noise in the reconstructed images (Fig. 3a). The Friedman test confirmed statistically significant differences in the residual noise achieved using the investigated filters ($\chi^2(6) = 60.0$, P-value = 4.50×10^{-11}; $n = 10$ paired images). The mean noise in the raw images (8.270 ± 0.225) was reduced by about 1.4 orders of magnitude by the Non-Local Means filter (to 0.32911 ± 0.01172), 3.1 orders of magnitude by the Bilateral filters (to 0.00961 ± 0.00038 by the Bilateral_0.05 filter, to 0.00402 ± 0.00020 by the Bilateral_0.1 filter), 3.2 orders of magnitude by the Wavelet filter (to 0.00540 ± 0.00046), and 4.5 orders of magnitude by the TV filters (to 0.000373 ± 0.000031 with TV_0.1, to 0.000169 ± 0.000006 with TV_0.2), corresponding to a mean noise reduction of 96.020% for the Non-Local Means filter, 99.884% and 99.951% for the Bilateral_0.05 and 0.1 filters, 99.935% for the Wavelet filter, and 99.995% and 99.998% for the TV_0.1 and 0.2 filters, respectively. The *post hoc* Wilcoxon signed-rank tests with Holm correction showed significant pairwise differences between conditions (adjusted P-value = 0.041 for all comparisons). The TV_02 filter reduced the inherent noise to a significantly lower level than all other filters and was used to de-noise all scanned images. The sequence of the pre-processing procedures (from smoothing to binarization) effectively improved the image quality (Fig. 3b–d), facilitating the identification, analysis and characterization of the various membranes in the 3D network and the digital reconstruction of the intermembrane pore architecture. Fig. 3e shows a still of the video with the 3D reconstruction of an exemplary ECS architecture in a VOI (SI video).

3.2 Characterization of pore distribution

Quantitative characterization of the complex geometry of the interconnected void architecture in the bioreactor ECS was challenging due to the various angles at which membranes were laid and the tilt angle of the bioreactor during scanning. In fact, the pores in the bioreactor ECS actually are the intermembrane voids in all coordinate directions. Due to their complex shape and the openness of the voids along the x and y coordinates, it was decided that possible sieving effects exerted by the 3D membrane network, in particular during cell seeding, could be better characterized with respect to the pore shape and size visible in bioreactor cross-sections parallel to the plane of the membrane mats (*i.e.*, the x–y plane) and orthogonal to the direction along which cells are seeded, as described below.

Fig. 4a and b show representative distributions of membranes and pores on surfaces orthogonal to the plane of the membrane mats (*i.e.*, the z–x and z–y planes). In Fig. 4a, the mats of the largest mPES TP membranes can be distinguished, overlaid on mats of the slightly smaller PP BO membranes. Thin polyester threads (not visible in the scans) held these membranes spaced at a distance that was more regular towards the bioreactor periphery and increased towards the bioreactor center (data not shown). This non-uniformity is likely caused by the manufacturing process, in which the membrane mats are manually stacked and bundled at the bioreactor periphery before casting the polyurethane housing around them. The microporous membranes were orderly arranged and held in fixed positions in the mats, with average intermembrane distances of about $\delta_{\mathrm{UMC}} = 241 \pm 144$ µm, $\delta_{\mathrm{DMC}} = 213 \pm 131$ µm, and $\delta_{\mathrm{BO}} = 207 \pm 134$ µm for the mPES membranes in the UMC and DMC and for the PP membranes, respectively (see Fig. 1 for the nomenclature). The smallest RC HD membranes are also clearly visible, physically holding TP and BO membranes in adjacent mats at a minimal vertical distance corresponding to one RC-HD membrane diameter. Their distribution is far less regular than those of the TP and BO membranes, because they were incorporated in the 3D membrane network as a loose bundle. Fig. 4a shows that the voids between the TP membranes (as well as the BO membranes) in the overlaid mats may be about 1.3 mm large, thereby defining large, highly interconnected intermembrane pores (or voids). These pores provide paths through which seeded cells may migrate, adhere on the available membrane surface, proliferate and differentiate. Fig. 4b shows that such

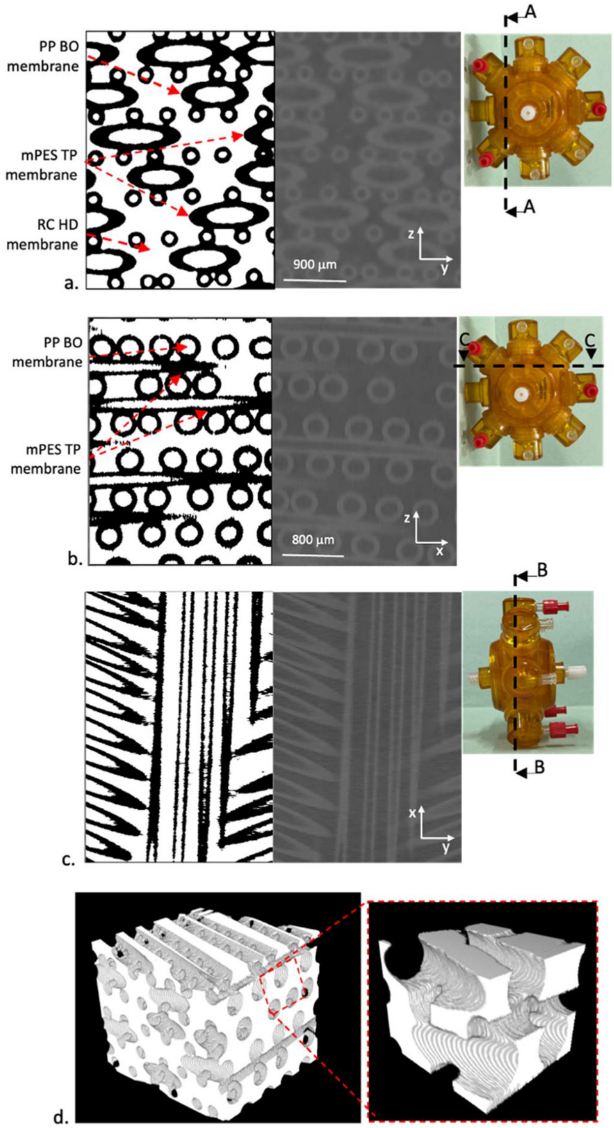

Fig. 4 Pore architecture in the BRx-HFMB ECS – description of the pore architecture of the BRx-HFMB ECS: (a–c) exemplary 2D cross-sectional images of BRx-HFMB ECS acquired by µCT at varying angles with respect to the planes of the membrane mats: left panel – thresholded and binarized image; centre panel – raw image; right panel – indication of the cross-sectional plane with respect to the plane of the membrane mats; and (d) 3D reconstruction of the pore architecture (*i.e.*, that of the voids) in the ECS.

large voids are interconnected by smaller channels, which may be a few tens of microns small, through which the medium permeating across the TP membranes may freely flow in all directions. Fig. 4c shows the distribution of membranes and pores over a surface parallel to the plane of a membrane mat. At any distance from the bioreactor top, the pores consisted of the voids among hollow fiber membranes bordered by the outer surfaces of the TP, BO and HD membranes. Their cross-sections were irregular, with the geometry and size depending on the type and arrangement of the membranes surrounding the pores and the position in the membrane network. Fig. 4d shows that the cross-sections of these pores were shaped as irregular cuboids, with the thickness approximately equal to one membrane diameter, and the width equal to the intermembrane distance in the given mat. Pores on planes parallel to the membrane mats were highly interconnected with the pores on orthogonal planes. The complex 3D shape of the ECS porosity and the very high degree of pore interconnectivity made it challenging to define a conventional pore structure from which the pore diameter could be estimated. For this reason, the ease with which cells and nutrients may migrate and move inside the 3D membrane network was characterized in terms of the width of the voids limiting their movement for any cross-sectional shape, *i.e.*, d_{pm}. Hence, the ECS mean pore diameter was defined as the mean intermembrane distance for long and thin slit pores (S) and as the mean diameter of the largest inscribed circle within rectangular pores (R). For the latter type of pores, d_{pm} was estimated to be 324 ± 82 µm. The quantitative architectural parameters obtained from the analysis of the reconstructed bioreactor images are reported in Fig. 5, 6 and Table 1. Although the investigated bioreactors were only prototypes, the analysis testifies to a good degree of manufacturing reproducibility.

Fig. 5a and b show that the statistical analysis did not reveal significant differences in the investigated parameters among the bioreactor quadrants. Hence, all architectural para-

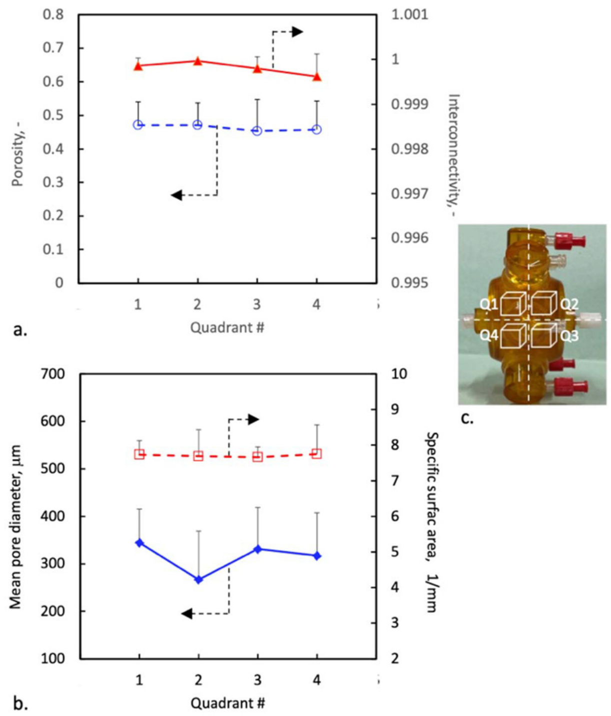

Fig. 5 Exemplary characteristics of the pore architecture of the BRx-HFMB ECS – parameters of the pore architecture of the BRx-HFMB ECS located in the membrane network in the different quadrants: (a) porosity and interconnectivity; (b) mean pore diameters of rectangular pores and specific surface areas; and (c) a panel showing the positions of the quadrants in the bioreactor. Differences were not statistically significant ($p < 0.05$).

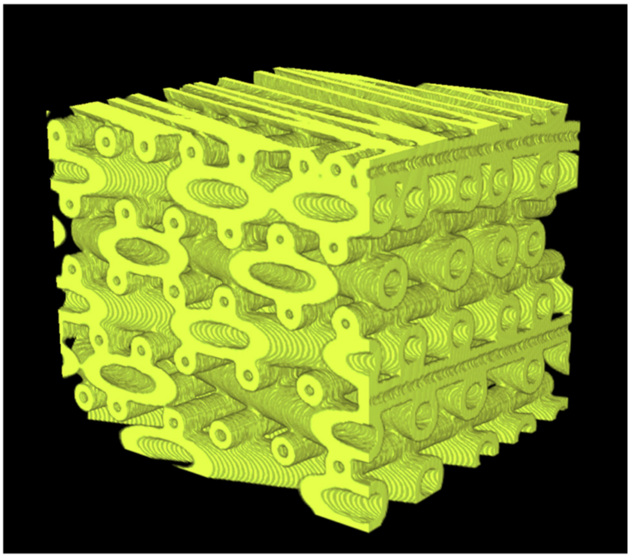

Fig. 6 Pore architecture of the BRx-HFMB – 3D CT reconstruction of the exemplary pore architecture in the extracapillary space of a BRx-HFMB showing the cell-scaffolding membrane surfaces and the intermembrane voids forming the pores through which cells migrate.

meters were statistically independent of the position and uniformly distributed inside the 3D membrane network. The Kruskal–Wallis test did not show statistically significant differences in porosity, interconnectivity, and specific surface area in the different quadrants (for porosity: $H = 0.562$, $p = 0.905$; for interconnectivity: $H = 1.531$, $p = 0.675$; and for specific surface area: $H = 0.085$, $p = 0.994$). The ECS porosity exhibited a ±2% maximal deviation from its mean value. The porosity was also about 20% higher than that of shell-and-tube HFMBs with densely packed membranes (HD-CW-HFMBs),[25] testifying to the BRx-HFMB capacity to host a greater mass of cells per unit volume. As shown in Fig. 4, the stacking of membrane mats and the varying orientation of membranes in overlaid mats generated a structure in which the pores in the ECS are highly interconnected. This is reflected in interconnectivity values close to 1 in all VOIs and bioreactor prototypes (Fig. 5a). The specific surface area exhibited a ±2% maximal deviation from its mean value and offered approximately 47% more membrane surface area for cell attachment than shell-and-tube HFMBs equipped with densely packed cross-woven membranes.

One-way ANOVA did not reveal statistically significant differences in the mean pore diameter in the various quadrants ($F(3196) = 1.72$, $p = 0.165$). The mean pore diameter varied with position in the 3D membrane network slightly more than other architectural parameters, with a ±17% maximal deviation from its mean value. This variability may be attributed to the different pore shapes on planes parallel and orthogonal to the membrane mats, inherent in the 3D network structure, and minor membrane rotations (Fig. 4c) or lateral displacements (Fig. 4a) occurring during the manual assembly of a bioreactor. These variations are not expected to significantly influence bioreactor performance. With a value of 272 ± 250 μm averaged over pores with different cross-sections, d_{pm} was slightly lower than that required for TE scaffolds.

However, considering the large pores parallel to the membrane mats interconnecting the pores orthogonal to the mats, and reflected in the high ECS pore interconnectivity, and of cell plasticity, it may be concluded that the 3D membrane network supports unhindered cell migration and the efficient transport of medium carrying nutrients, oxygen and biochemical cues throughout the BRx-HFMB ECS. Taken together, the architectural parameters suggest that BRx-HFMBs are slightly better suited than shell-and-tube HFMBs for the culture of tissues with high cellularity (*i.e.*, the number of cells per unit tissue volume), such as the liver and some tumors.

It is worth noting that membrane wetting or cell proliferation and differentiation may potentially change the ECS architectural parameters with respect to those herein reported. Different from other HFMBs, the membrane materials used for the BRx-HFMB (*e.g.*, PES and PP) are rather hydrophobic, but for the cellulosic membranes used for supplying additional biochemical cues. As a result, wetting, with the associated water absorption and membrane swelling, may be expected to cause negligible volumetric changes of the ECS and its architectural parameters. More importantly, as the tissue matures, cells proliferate and differentiate and may fill in the voids in the ECS with new cells or the self-secreted ECM, which is later mineralized. This may dramatically decrease all architectural parameters. In case the bioreactor is dynamically operated, such reduction may increase the hydraulic resistance of the bioreactor ECS to such an extent that the medium can no longer flow through the cell construct and solute transport to/away from cells occurs purely by diffusion. Consequently, unless new vessels have formed inside constructs with near-physiological cell density, as was reported for cells from the

Table 1 Architectural parameters of the pore (*i.e.*, void) distribution in the ECS of BRx-HFMBs compared to: a shell-and-tube HFMB prepared with rolled cross-woven mats of densely packed HF membranes (HD-CW HFMB), a synthetic narrow pore hydroxyapatite (NPHA) scaffold commercialized as a bone substitute, and a natural equine femur trabecular bone (EFT). S refers to slit pores and R refers to pores with rectangular cross sections

	BRx-HFMB	HD-CW HFMB[36]	Synthetic NPHA scaffold[52]	Natural EFT[52]	Humann trabecular bone
Porosity, %	46 ± 6	45.8 ± 0.01	73 ± 0.35	65 ± 0.38	45–87[66,67]
Pore interconnectivity, %	100	99	100	100	
Specific surface area, mm^{-1}	7.71 ± 0.45	5.71 ± 0.05	9.38 ± 0.1	8.05 ± 0.67	3–30[68,69]
Mean pore size, μm	324 ± 82/R 220 ± 236/S	303 ± 4	416 ± 211	433 ± 194	200–300[66]

liver digest cultured in BRx-HFMBs in dynamic operation, anoxic zones might establish in the construct, which in time may cause cell necrosis far away from the oxygen source.

3.3 Biomimicry of pore distribution

The extent to which the ECS void distribution in BRx-HFMBs mimics the bone tissue ECM was assessed with respect to natural equine femur trabecular bone tissue and a commercial synthetic narrow pore hydroxyapatite (NP-HA) scaffold available as a bone substitute and for bone TE. As shown in Table 1, the architectural parameters of BRx-HFMB prototypes closely mimic those of the reference benchmarks. The ECS mean porosity was slightly lower than those of the benchmarks, being approximately 19% lower than that of natural equine femur trabecular bone and approximately 25% lower than that of the NP-HA scaffold.[41] The mean ECS pore diameter was about 36% smaller than those of the benchmarks and only 9% lower on average than the commonly agreed lower limit of 300 μm required to ensure unhindered cell migration throughout TE scaffolds. Fig. 4d and 6 show that the ECS voids in BRx-HFMBs form smooth-surfaced pores resulting from the intersections of voids on surfaces parallel and orthogonal to the plane of the membrane mats. Such a complex and regular pore shape bears little resemblance to that of the pores bordered by the flat and irregularly curved *trabeculae* of the natural bone. Yet, the pores in the BRx-HFMB ECS are as highly interconnected through large pores as those in the natural bone tissue and exhibit a comparable specific surface area for cell attachment.

All architectural parameters of the BRx-HFMB met the general requirements for scaffolds suitable for TE, supporting their feasibility for TE applications. Today, BRx-HFMBs are commercially available that are only equipped with membranes similar in size and separation properties, and mats similar in membrane density, to those investigated in this study. On purely speculative grounds, varying the membrane diameter and density in space at will, and the assembly of membranes in the bioreactor, might enable the production of BRx-HFMBs with an ECS architecture mimicking the ECM of natural tissues other than the bone.[70] For example, a BRx-HFMB with an ECS with an average pore size range of 25–60 μm could be developed for myocardial tissue regeneration. The layered nature of the 3D membrane network could even make it possible to produce an ECS with hierarchical gradients of porosity and pore size. A stack of three membrane layers could be engineered to mimic the skin where the average pore size in each layer should increase from a few microns (possibly consisting of one flat microporous membrane mimicking the epidermis) to a few tens of microns (to mimic the dermis), up to a few hundreds of microns (to mimic the layer supporting hair follicles and blood vessels). It remains to be seen whether suitable membranes and a membrane assembling technique are available that make bioreactor production technically feasible and sustainable.

Interestingly, the architectural analysis showed that in the 3D membrane network the maximal observed distance between membranes of the same type (*i.e.*, mPES or PP) may exceed 1 mm, about ten times the maximum distance from the oxygen source tolerable for cell survival under static culture conditions. Evidence in the literature shows that cells (*e.g.*, primary liver cells[71,72]) may enter the 3D membrane network of BRx-HFMBs and may migrate and colonize the voids in the ECS, as shown in Fig. 7. Nevertheless, evidence is also available showing that, when they are cultured in the BRx-HFMB, cells with high oxygen metabolic requirements, such as primary liver cells, survive, differentiate and function for weeks at near-physiological cell concentrations.[49–51] Integrating the information gathered in this study on the 3D membrane network architecture with the similarity to the morphology and functions of mature cell constructs in the BRx-HFMB with natural liver tissue suggests that the positive effects of the ECS architecture in such bioreactors go beyond the architectural resemblance to natural tissue (*i.e.*, "structural biomimetics"). It could be speculated that the presence of many membranes densely distributed in the 3D network structure that deliver medium and oxygen to cells may play an important role. In fact, all membranes bordering the ECS pores supply oxygen either convectively through the oxygen-rich medium permeating the TP membranes or by diffusion from the oxygen-rich gas

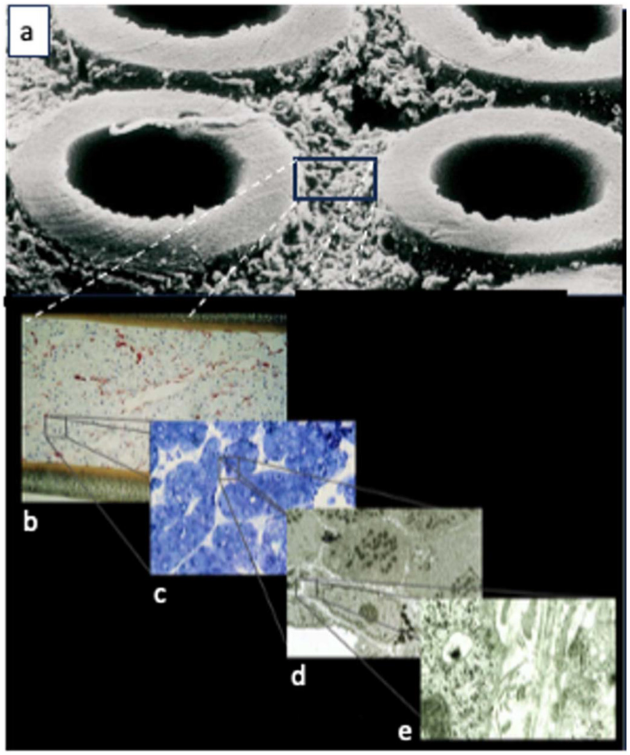

Fig. 7 Liver cell distribution and organization among the hollow fibre membranes in the 3D network of a BRx-HFMB: (a) cells densely proliferated and packed among membranes; (b) primary human liver cells in high density co-culture between two artificial membranes; (c) hepatocytes spontaneously aggregating and non-parenchymal cells forming channels; (d) re-formation of neo-liver sinusoids; and (e) stellate cells that produce a biomatrix in a neo-space of Disse. Details in ref. 71 and 72.

flowing in the BO membranes (Fig. 4a). Definitely, convection-enhanced oxygen transport may have an effect, as in the case of other dynamic bioreactors, but likely only at the beginning of culture. Perfusion of cells co-cultured in the BRx-HFMB with endothelial cells may even promote the formation of neo-vessels in the construct perpendicular to the membrane mats that further relieve the limitations to oxygen transport in mature hydraulically resistant cell constructs.[49–51] Biomimetic ECS, cell perfusion with medium, and optimal spatial distribution of many oxygen sources may all contribute to overcoming the limitations to oxygen transport to densely packed cells with high oxygen demand seeded into the BRx-HFMB ECS and may enable their culture in a viable and functional state for weeks, as has been reported for liver cells. In the case of bone cells, the fluid-mechanical stimulation associated with construct perfusion might have the additional benefit of promoting osteogenic cell differentiation into osteoblasts and the synthesis and mineralization of the bone ECM.[28,73] In summary, in the culture of mechano-sensitive cells with high nutrient and oxygen metabolic demands, like bone cells, the 3D membrane network in BRx-HFMBs may offer the seeded cells a porous ECS architecture mimicking the bone-specific ECM and an efficient way to supply cells with oxygen resembling that of natural bone (*i.e.*, "functional biomimetics"). Optimal operating conditions might exploit the peculiar bioreactor characteristics to promote neo-vessel formation and to generate culture conditions mimicking the bone microenvironment. Such optimization could be supported by computational models of dynamic oxygen transport and metabolic processes and evolution of the cell populations and would have to be validated in cell culture experiments. However, it should be noted that to optimize the bioreactor design (*i.e.* its structure and operating conditions) a more extensive architectural characterization study would help than that herein reported. Its sustainability for a given application should also be evaluated.

It is worth noting that current BRx-HFMBs are equipped with non-biodegradable, non-bioresorbable membranes; hence they are best suited for applications in which the engineered tissue is not implanted. Consequently, today the advantageous characteristics of BRx-HFMBs may be better exploited in bioartificial organs for extracorporeal support to patients with severe metabolic insufficiency, or in *in vitro* tissue/organ models for personalized medicine. Evidence in the literature suggests that the co-culture of primary cells from digested livers in BRx-HFMBs could provide acute liver failure patients with the missing liver metabolic functions until their own liver regeneration. For similar reasons, mechanosensitive osteogenic cells with similarly demanding oxygen requirements could be profitably cultured in BRx-HFMBs to develop cellular models of bone tissue to screen drug toxicity and effectiveness.

4. Conclusions

The BRx-HFMB has been successfully used for the co-culture of large masses of cells with high oxygen and nutrient demands. Yet a quantitative characterization study of the architecture of its extra-capillary space is still lacking. In this study the ECS architecture of BRx-HFMB prototypes was characterized by high-resolution μCT coupled with advanced AI-based image analysis. The analysis showed that the pore architecture of the BRx-HFMB ECS exhibits a consistent and spatially uniform pore structure that mimics the natural bone ECM and may favour migration through, and adhesion on, the membranes in the 3D network of a large clinical-scale cell mass. The large intermembrane gaps in the ECS and the good performance reported for BRx-HFMBs in the co-culture of cells with high oxygen and nutrient demands suggest that the architecture of the 3D membrane network contributes to bioreactor performance also through the dense spatial distribution of membranes that effectively supply cells with medium, oxygen and nutrients. These features qualify the BRx-HFMB as a suitable candidate for developing cellular models of bone tissue for drug testing and precision medicine. The next step of the work will be to model the transport of oxygen and relevant solutes in bioreactors seeded with osteogenic cells instrumental in the optimization of bioreactor design for this application.

Author contributions

Giuseppe Falvo D'Urso Labate (GFDL): conceptualization, data curation, formal analysis, funding acquisition, investigation, and writing – original draft; Chiara Morano (CM): data curation, formal analysis, investigation, visualization; and writing – original draft; Thomas De Schryver (TDS): investigation; Harry Zaverdas (HZ): data curation, software; and visualization; Luigi De Napoli (LDN): formal analysis; visualization; supervision; Gionata Fragomeni (GF): data curation; formal analysis; investigation, and writing – original draft; Luc Van Hoorebeke (LVH): methodology, resources, and supervision; Patrick Segers (PS): funding acquisition and supervision; Matthieu N. Boone (MB): methodology, resources, and supervision; Konstantinos Theophilatos (KT): funding acquisition, methodology, resources, software, and supervision; Joerg C. Gerlach (JCG): formal analysis, funding acquisition, and supervision; Gerardo Catapano (GC): conceptualization, formal analysis, funding acquisition, methodology, supervision, and writing – original draft; all authors: writing – review & editing.

Conflicts of interest

One of the authors (JCG) declares owning stocks of the firm Hybrid Organ GmbH. All other authors declare that they have no known competing financial interests or personal relationships that could have appeared to influence the work reported in this paper.

Data availability

The software developed for this study is available in the GitHub repository (https://github.com/InSyBio-PC/bioreactor_ image_analysis). The 3D reconstruction of an exemplary VOI in the BRx-HFMB, the 2D reconstructed images used for the VOI reconstruction, the estimation of the mean pore size, and the fine tuning of the filter for image denoising are available in the Zenodo (https://doi.org/10.5281/zenodo.18324010) repository. Other data will be made available upon request subject to permission from Hybrid Organ GmbH.

Supplementary information (SI): Fig. S1 – schematic workflow of the de-noising sequential procedures, and supplementary video – 3D VOI reconstruction in the BRx-HFMB ECS. See DOI: https://doi.org/10.1039/d6bm00185h.

Acknowledgements

This study was funded by the European Community through the OSTEONET project, under the Horizon Europe Marie Sklodowska-Curie Actions Staff Exchange programme, grant agreement no. 101086329, the Italian Ministero dell'Università e della Ricerca through the project SAISEI, within the framework of the PRIN 2022 program (D.D.104–02/02/2022), and the Special Research Fund of Ghent University (BOF-UGent) for the support to the UGCT Core Facility (BOF.EXP.2017.0007 and BOF.COR.2022.008). This manuscript reflects only the authors' views and opinions, and the Italian Ministry cannot be held responsible for them. The authors gratefully acknowledge Hybrid Organ GmbH, Berlin, Germany, for kindly providing the bioreactor prototypes used for this study.

References

1 R. A. Knazek, P. M. Gullino, P. O. Kohler and R. L. Dedrick, *Science*, 1972, **178**(4056), 65–66, DOI: 10.1126/science.178.4056.65.
2 N. Wung, S. M. Acott, D. Tosh and M. J. Ellis, *Biotechnol. Lett.*, 2014, **36**(12), 2357–2366, DOI: 10.1007/s10529-014-1619-x.
3 C. Charcosset, *Int. J. Membr. Sci. Technol.*, 2016, **3**, 22–38.
4 S. M. Yoo, V. W. C. Lau, C. Aarts, B. Bojovic, G. Steinberg, J. A. Hammill, A. Dvorkin-Gheva, R. Ghosh and J. L. Bramson, *OncoImmunology*, 2021, **10**(1), 1995168, DOI: 10.1080/2162402X.2021.1995168.
5 Y. Hou, K. Mi, L. Sun, K. Zhou, L. Wang, L. Zhang, Z. Liu and L. Huang, *Pharmaceutics*, 2022, **14**, 1485, DOI: 10.3390/pharmaceutics14071485.
6 S. G. Garcia, M. Sanroque-Muñoz, M. Clos-Sansalvador, M. Font-Morón, M. Monguió-Tortajada, F. E. Borràs and M. Franquesa, *Extracellular Vesicles Circ. Nucleic Acids*, 2024, **5**, 201–220, DOI: 10.20517/evcna.2023.76.
7 G. Catapano, P. Czermak, R. Eibl, D. Eibl and R. Pörtner, *Cell Tissue React. Eng.*, 2009, 217–241.
8 T. U. Rahman, H. Roy, M. R. Islam, M. Tahmid, A. Fariha, A. Mazumder, N. Tasnim, M. N. Pervez, Y. Cai and V. Naddeo, *Membranes*, 2023, **13**, 181, DOI: 10.3390/membranes13020181.
9 S. Judd, 2024, https://www.thembrsite.com/features/hollow-fiber-mbr-membrane-modules-commercial-products, accessed on November 14, 2025.
10 J. S. John, C. Whitford and W. G. Whitford, *Technology Platforms for 3D Cell Culture, Chapter 14*, 2017 pp.327–350, DOI: 10.1002/9781118851647.ch14.
11 Z. Sadouki, T. D. McHugh, R. Aarnoutse, J. Ortiz Canseco, C. Darlow, W. Hope, J. van Ingen, C. Longshaw, D. Manissero, A. Mead, L. Pelligand, L. Phee, J. Readman, M. M. Ruth, J. F. Standing, N. Stone, E. Q. Wey and F. Kloprogge, *J. Antimicrob. Chemother.*, 2021, **76**, 2252–2259, DOI: 10.1093/jac/dkab160.
12 P. Chan and K. W. Leong, *Eur. Spine J.*, 2008, **17**(Suppl. 4), S467–S479, DOI: 10.1007/s00586-008-0745-3.
13 S. P. S. Monga, M. S. Hout, M. J. Baun, A. Micsenyi, P. Muller, L. Tummalapalli, A. R. Ranade, J.-H. Luo, S. C. Strom and J. C. Gerlach, *Am. J. Pathol.*, 2005, **167**(5), 1279–1292.
14 C. Pekor, J. C. Gerlach, I. Nettleship and E. Schmelzer, *Tissue Eng. Part C Methods*, 2015, **21**(7), 705–715, DOI: 10.1089/ten.tec.2014.0453.
15 M. A. Fernandez-Yague, S. A. Abbah, L. McNamara, D. I. Zeugolis, A. Pandit and M. J. Biggs, *Adv. Drug Delivery Rev.*, 2015, **84**, 1–29, DOI: 10.1016/j.addr.2014.09.005.
16 V. Karageorgiu and D. Kaplan, *Biomaterials*, 2005, **26**, 5474–5491.
17 Y. Du, J. L. Guo, J. Wang, A. G. Mikos and S. Zhang, *Biomaterials*, 2019, **218**, 119334, DOI: 10.1016/j.biomaterials.2019.119334.
18 S. S. Lee, X. Du, I. Kim and S. J. Ferguson, *Matter*, 2022, **5**, 2722–2759, DOI: 10.1016/j.matt.2022.06.003.
19 E. A. Todd, *et al.*, *J. Funct. Biomater.*, 2024, **15**(10), 280, DOI: 10.3390/jfb15100280.
20 A. C. Sousa, *et al.*, *Biomater. Adv.*, 2025, **166**, 214042, DOI: 10.1016/j.bioadv.2024.214042.
21 S. Chen and M. Wang, *Adv. Mater. Technol.*, 2026, e01877, DOI: 10.1002/admt.202501877.
22 Y. Ha, *et al.*, *Adv. Funct. Mater.*, 2022, **32**, 2200011, DOI: 10.1002/adfm.202200011.
23 T. O. Josephson and E. F. Morgan, *Front. Physiol.*, 2023, **14**, 1232698, DOI: 10.3389/fphys.2023.1232698.
24 S. Hao, M. Wang, Z. Yin, Y. Jing, L. Bai and J. Su, *Mater. Today Bio*, 2023, **22**, 100741, DOI: 10.1016/j.mtbio.2023.100741.
25 L. Dalle Carbonare, *et al.*, *Stem Cell Res. Ther.*, 2025, **16**, 169, DOI: 10.1186/s13287-025-04288-4.
26 C. Lu, *et al.*, *Bone*, 2013, **52**(1), 220–229, DOI: 10.1016/j.bone.2012.09.037.
27 S. S. Hannah, S. McFadden, A. McNeilly and C. McClean, *J. Cell Physiol.*, 2021, **236**(2), 721–740, DOI: 10.1002/jcp.29921.
28 I. E. De Napoli, S. Scaglione, P. Giannoni, R. Quarto and G. Catapano, *J. Membr. Sci.*, 2011, **379**, 341–352.
29 T. J. Chresand, D. J. Gillies and B. E. Dale, *Biotechnol. Bioeng.*, 1988, **32**, 983–992.
30 H. Ye, D. B. Das, J. Triffit and Z. F. Cui, *J. Membr. Sci.*, 2006, **272**, 169–178.

31 A. J. Davidson, M. J. Ellis and J. B. Chaudhuri, *Biotechnol. Bioeng.*, 2010, **106**(6), 980–988.

32 L. J. Kelsey, M. R. Pillarella and A. L. Zydney, *Chem. Eng. Sci.*, 1990, **45**(11), 3211–3220.

33 J. D. Brotherton and P. C. Chau, *Biotechnol. Prog.*, 1996, **12**, 575–590.

34 J. Koska, B. D. Bowen and J. M. Piret, *Chem. Eng. Sci.*, 1997, **52**(14), 2251–2263.

35 I. E. De Napoli, E. M. Zanetti, G. Fragomeni, E. Giuzio, A. L. Audenino and G. Catapano, *J. Membr. Sci.*, 2014, **471**, 347–361.

36 G. Falvo D'Urso Labate, *et al.*, *J. Membr. Sci.*, 2022, **650**, 120403, DOI: 10.1016/j.memsci.2022.120403.

37 J. C. Gerlach, K. Zeiliger and J. F. Patzer II, *Regener. Med.*, 2008, **3**(4), 575–595, DOI: 10.2217/17460751.3.4.575.

38 G. Catapano, Bioreactors for bioartificial organs, in *Cell and Tissue Reaction Engineering*, ed. R. Eibl, D. Eibl, R. Pörtner, G. Catapano and P. Czermak, Springer-Verlag, Berlin Heidelberg, 2009, pp. 279–314.

39 J. C. Gerlach, J. Encke, O. Hole, C. Müller, J. M. Courtney and P. Neuhaus, *Int. J. Artif. Organs*, 1994, **17**, 301–306.

40 U. Baurmeister, USPatent 1992, 5,141,031 Akzo N.V., The Netherlands.

41 G. Catapano, A. Wodetzki and U. Baurmeister, *Int. J. Artif. Organs*, 1992, **15**(4), 327–330.

42 J. C. Gerlach, *Cell Transplant.*, 2006, **15**(1), S91–S103.

43 J. C. Gerlach, *et al.*, *Cells. Tissues. Organs*, 2010, **192**(1), 39–49, DOI: 10.1159/000291014.

44 J. C. Gerlach, *et al.*, *Tissue Eng., Part C*, 2010, **16**(1), 15–21, DOI: 10.1089/ten.

45 T. Miki, A. Ring and J. Gerlach, *Tissue Eng., Part C*, 2011, **17**(5), 557–568, DOI: 10.1089/ten.TEC.2010.0437.

46 H. Stachelscheid, *et al.*, *J. Tissue Eng. Regen. Med.*, 2013, **7**(9), 729–741, DOI: 10.1002/term.1467.

47 F. Knospel, *et al.*, *Biotechnol. Prog.*, 2016, **32**(1), 141–151, DOI: 10.1002/btpr.2182.

48 F. Meier, *et al.*, *Int. J. Mol. Med.*, 2017, **40**(6), 1759–1771, DOI: 10.3892/ijmm.2017.3190.

49 J. C. Gerlach, *et al.*, *Int. J. Artif. Organs*, 2001, **24**, 793–798.

50 Y. Sakai, *et al.*, *Cell Transplant.*, 1999, **8**(5), 531–541, DOI: 10.1177/096368979900800508.

51 I. M. Sauer, *et al.*, *Int. J. Artif. Organs*, 2002, **25**, 1001–1005.

52 G. Falvo D'Urso Labate, *et al.*, *J. Appl. Biomater. Funct. Mater.*, 2016, **14**(3), e277–e289.

53 K. Zeilinger, *et al.*, *Tissue Eng., Part C*, 2011, **17**(5), 549–556, DOI: 10.1089/ten.TEC.2010.0580.

54 B. Masschaele, *et al.*, *J. Phys.: Conf. Ser.*, 2013, **463**, 012012, DOI: 10.1088/1742-6596/463/1/012012.

55 C. A. Schneider, W. S. Rasband and K. W. Eliceiri, *Nat. Methods*, 2012, **9**, 671–675, DOI: 10.1038/nmeth.2089.

56 S. Van Der Walt, *et al.*, *Peer J.*, 2014, **2**, e453.

57 G. Bradski, The OpenCV Library, *Dr Dobbs J. Softw. Tools*, 2000, **120**, 122–125.

58 T. Barbu, *Appl. Anal.*, 2013, 1–8.

59 S. Iqbal, T. M. Khan, K. Naveed, S. Naqvi and S. J. Nawaz, *Comput. Biol. Med.*, 2022, **151**, 106277.

60 N. Otsu, *IEEE Trans. Syst. Man Cybern. Syst.*, 1979, **9**, 62–66.

61 L. I. Rudin, S. Osher and E. Fatemi, *Phys. D*, 1992, **60**, 259–268.

62 C. Tomasi and R. Manduchi, International Conference on Computer Vision (IEEE Cat. No.98CH$_3$6271), 839–846, DOI: 10.1109/ICCV.1998.710815.

63 F. Banterle, *et al.*, *Comput. Graph. Forum*, 2012, **31**, 19–32.

64 C. Zanchettin and T. B. Ludermir, *Appl. Soft Comput.*, 2007, **7**, 246–256.

65 A. Buades, B. Coll and J.-M. Morel, IEEE Computer Society Conference on Computer Vision and Pattern Recognition (CVPR'05), 2005, 2, 60–65.

66 T. Doktor, J. Valach, D. Kytýř and O. Jiroušek, 17th International Conference ENGINEERING MECHANICS 2011, Svratka, Czech Republic, 9–12 May 2011.

67 A. A. R. Rabiatul, *et al.*, *Biomech. Model. Mechanobiol.*, 2021, **20**(3), 957–968, DOI: 10.1007/s10237-021-01423-x.

68 A. H. Beddoe, *Calcif. Tissue Res.*, 1978, **25**, 273–281.

69 G. A. P. Renders, L. Mulder, L. J. van Ruijven and T. M. G. J. van Eijden, *J. Anat.*, 2007, **210**, 239–248, DOI: 10.1111/j.1469-7580.2007.00693.x.

70 F. Mukasheva, L. Adilova, A. Dyussenbinov, B. Yernaimanova, M. Abilev and D. Akilbekova, *Front. Bioeng. Biotechnol.*, 2024, **12**, 1444986, DOI: 10.3389/fbioe.2024.1444986.

71 J. C. Gerlach, N. Schnoy, J. Encke, M. D. Smith, C. Muller and P. Neuhaus, *Hepatology*, 1995, **22**(2), 546–552. Epub 1995/08/01. PubMed PMID: 7635423.

72 M. Okamoto, *et al.*, *Hepatology*, 1997, **26**(4), 575A.

73 C. Wittkowske, *et al.*, *Front. Bioeng. Biotechnol.*, 2016, **4**, 87, DOI: 10.3389/fbioe.2016.00087.